



Contents lists available at ScienceDirect

## Journal of the Mechanics and Physics of Solids

journal homepage: [www.elsevier.com/locate/jmps](http://www.elsevier.com/locate/jmps)

# Compressive response of a sandwich plate containing a cracked diamond-celled lattice

I. Quintana Alonso, N.A. Fleck\*

Cambridge University, Department of Engineering, Trumpington Street, Cambridge CB2 1PZ, UK

## ARTICLE INFO

## Article history:

Received 10 December 2008

Received in revised form

4 May 2009

Accepted 10 May 2009

## Keywords:

Fracture mechanics

Buckling

Finite element method

Defect sensitivity

## ABSTRACT

The compressive strength is determined for a sandwich plate containing a centre-cracked core made from an elastic–brittle, diamond-celled lattice. It is assumed that the lattice fails when the major component of principal stress anywhere in the lattice attains the compressive or tensile strength of the solid, or when local buckling intervenes. First, analytical and numerical predictions are given for the unnotched strength of the core and for the compressive fracture toughness of the lattice  $K_{IC}$ . Second, finite element simulations and analytical models are reported for the fracture response of the sandwich plate with cracked core. The active failure mechanism in the cracked core is sensitive to core height, crack length, lattice geometry and material choice; this is illustrated by means of material-property charts.

© 2009 Elsevier Ltd. All rights reserved.

## 1. Introduction

Lattice materials are candidate materials for the cores of sandwich plates: they are light, stiff, and strong. A wide range of core topologies and cell-wall materials now exist. For example, sandwich plates comprising a ceramic square honeycomb core have multifunctional application involving high temperature and resistance to thermal shock, in addition to high stiffness and strength per unit mass. These structures are used as catalytic converters and diesel particulate filters for automobiles, medical prosthetic implants, absorbers for solar energy and as lightweight supports for satellites. In-service damage by cracking arises as a result of the severe thermo-mechanical loads, with a reduction in fracture strength (Gulati, 1983). There is a clear need to understand the defect tolerance of these structures.

A range of lattice topologies exist and their multifunctional properties have already been demonstrated (see the review by Wadley, 2006). For example, the diamond-celled lattice has found industrial application (Gulati, 1975; Scheffler and Colombo, 2005). Recently, Côte et al. (2006) have used numerical and experimental methods to investigate the compressive and shear responses of a metallic diamond core. Valdevit et al. (2004) carried out a structural optimisation of the diamond-celled lattice in a sandwich plate configuration, and compared its behaviour with plates designed using competing topologies such as truss or honeycomb cores. They concluded that the diamond core is the lightest topology for combined load bearing and active cooling application.

There has been significant research activity on the stiffness and strength of a wide range of 2D and 3D lattices. The in-plane elastic properties of various lattice topologies are now well understood (Gibson and Ashby, 1997; Christensen, 2000; Wang and McDowell, 2004). Less is known about their fracture toughness. The concept of fracture toughness  $K_{IC}$  is based upon the existence of a  $K$ -field on a length scale much greater than the cell size of the lattice. For an elastic, brittle lattice

\* Corresponding author. Tel.: +44 1223 748240; fax: +44 1223 765046.

E-mail address: [naf1@cam.ac.uk](mailto:naf1@cam.ac.uk) (N.A. Fleck).

the value of  $K_{IC}$  is determined by assuming that the critical strut directly ahead of the crack tip fails when the maximum tensile stress within it attains the tensile fracture strength  $\sigma_{TS}$  of the solid cell walls. Several authors have determined the fracture toughness of planar lattices using both analytical and numerical techniques (see for example Lipperman et al., 2007; Romijn and Fleck, 2007). For the diamond lattice of the present study, mode I fracture toughness depends upon the cell size  $l$ , the thickness of the struts  $t$ , and the tensile strength of the solid material  $\sigma_{TS}$  according to (Quintana-Alonso and Fleck, 2007a)

$$\tilde{K}_{IC} = 0.44tl^{-1/2}\sigma_{TS} \quad (1)$$

The available experimental data (Huang and Gibson, 1991; Quintana-Alonso et al., 2009) support Eq. (1).

The flaw sensitivity of *lattice structures* has not yet been explored, but is of practical interest by the following illustration. Consider the prototypical geometry of a centre-cracked plate (CCP) with a crack length  $2a$  and subjected to the remote tensile stress  $\sigma_u$ . In the absence of a crack, the unnotched tensile strength  $\sigma_u$  of the diamond-celled lattice plate is given by  $\sigma_u = 2t^2\sigma_{TS}/(3l^2)$ . Alternatively, when a long crack is present the strength is dictated by the linear elastic fracture mechanics criterion  $K_I = \tilde{K}_{IC}$ , where  $K_I$  is the applied stress intensity factor. Consequently, there exists a transition in behaviour from strength-control to toughness-control at the transition flaw size  $a_T = \tilde{K}_{IC}^2/\pi\sigma_u^2$  (Fleck et al., 1994). The tensile strength is on the order of  $\sigma_u$  for  $a < a_T$ , while it is on the order of  $\tilde{K}_{IC}/\sqrt{\pi a}$  for  $a > a_T$ .

The above analysis is modified somewhat for the case of a sandwich plate with core made from a pre-cracked lattice material. Quintana-Alonso and Fleck (2007b) have explored the *tensile* strength of a cracked sandwich core of geometry shown in Fig. 1; the diamond core is of height  $2H$  and contains a centre-crack of length  $2a$ . They assumed that the operative failure mechanism is local tensile fracture of the most heavily stressed material element within the lattice. At small values of  $Ht/l^2$ , there is a negligible stress concentration due to the presence of the centre-crack, and the net tensile strength is given by the unnotched strength of the lattice core,  $\sigma_u^T$ . (Note that the presence of the face-sheets constrains the lattice against Poisson contraction, and thereby elevates  $\sigma_u^T$  to the value  $\sigma_u^T = \sigma_{TS}t/l$  which exceeds  $\sigma_u$ ). At large values of  $Ht/l^2$ , a  $K$ -field exists ahead of the crack tip, and the tensile strength of the sandwich panel is dictated by the tensile fracture toughness of the lattice. Consequently, the tensile strength of the centre-cracked lattice core can be expressed in terms of the two tensile fracture parameters ( $\sigma_u^T, \tilde{K}_{IC}$ ). In service, the core of a sandwich panel is typically loaded by a combination of compression and shear. The defect tolerance of a core under compressive loading is the subject of the current study, while the case of remote shear will be dealt with separately.

### 1.1. Statement of the problem

The aim of the current study is to investigate the *compressive* fracture response of a sandwich plate made from an elastic-brittle lattice and containing a centre-crack, as already defined in Fig. 1. The plate is of width  $2W$ , and the lattice core has square cells oriented at  $\omega = \pm 45^\circ$  with respect to the rigid face-sheets, resembling a “wine-box” arrangement. Compressive loading is applied normal to the face-sheets by imposing a remote compressive stress  $\sigma_\infty$ , based upon the gross cross-section.

The relative density  $\bar{\rho}$  of the diamond-celled lattice, defined as the density of the lattice divided by that of the solid from which the cell walls are made, is given by

$$\bar{\rho} = \frac{2t}{l} - \left(\frac{t}{l}\right)^2 \quad (2)$$

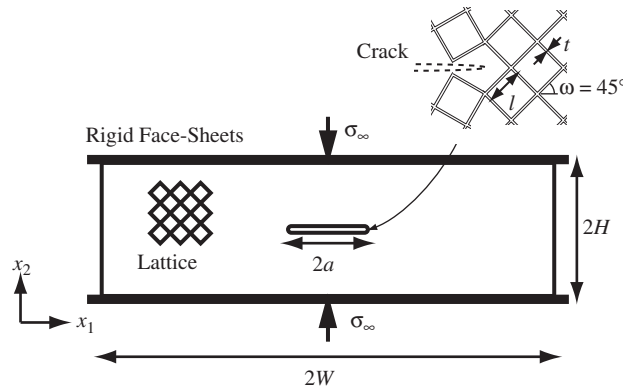


Fig. 1. Sandwich plate containing a cracked diamond lattice core, and subjected to compressive loading.

In the ensuing analysis, the cell walls of the lattice are made from a linear-elastic solid material of Young's modulus  $E_s$ , tensile fracture strength  $\sigma_{TS}$ , and compressive fracture strength  $\sigma_{CS}$ . Failure of the centre-cracked sandwich core occurs by the following competing mechanisms:

- (i) maximum compressive stress at any point in the lattice attains the value  $\sigma_{CS}$ ,
- (ii) maximum tensile stress at any point in the lattice attains the value  $\sigma_{TS}$ , or
- (iii) cell walls buckle elastically.

Dimensional analysis dictates that the normalised fracture strength  $\sigma_\infty/\sigma_{TS}$  of the cracked sandwich plate is a function of the non-dimensional geometric groups ( $t/l$ ,  $a/l$ ,  $H/l$ ,  $H/W$ ) and of the material groups ( $\sigma_{CS}/\sigma_{TS}$ ,  $\sigma_{TS}/E_s$ ). We shall explore the dependence of the fracture strength  $\sigma_\infty/\sigma_{TS}$  upon these groups, and limit attention to the practical geometries where  $H/W \ll 1$ . It is recognised that stress concentrations also arise at the free edges, but these are ignored as the focus of the investigation is upon the reduction in strength due to a centre-crack in the sandwich plate.

### 1.2. The concept of a compressive fracture toughness

The notion of a *compressive fracture toughness* is extensively employed in this paper. This is made precise as follows. A buckling fracture toughness  $K_{IC}^B$  is dictated by local elastic buckling at the crack tip of a traction-free crack. Crack tip failure can also occur by the attainment of a local compressive fracture stress  $\sigma_{CS}$  in the most heavily loaded strut near the crack tip: this local failure criterion defines an alternative compressive fracture toughness  $K_{IC}^C$ . A third possibility is local tensile failure when the maximum local tensile stress attains the value  $\sigma_{TS}$ ; the corresponding fracture toughness is denoted by  $K_{IC}^T$ . The compressive fracture toughness  $K_{IC} = \min(K_{IC}^B, K_{IC}^C, K_{IC}^T)$ .

It is recognised that the crack faces approach each other under compressive loading, and so a finite compressive stress intensity factor cannot be generated for the case of a mathematical line crack of zero initial opening. In this study we envisage that initial defects exist in the form of sharp notches, with tip acuity defined by the lattice cell size. Consequently, the crack will remain open under applied compressive loading, and a stress intensity will be generated. If crack face contact does occur the crack face tractions will be small due to the low 'rubble strength' of the failed lattice, by the following argument. An increasing crack face overlap is associated with the random failure of struts which come into contact stochastically: at any instant the compressive traction across the crack faces will be supported by only a few contacting struts, and the compressive strength is thereby small. A similar argument has been made by [Mora and Waas \(2002\)](#) for the compressive strength of ceramic foams. We conclude that the concept of compressive fracture toughness has a sound physical basis.

### 1.3. Outline of the study

First, the unnotched strength of the sandwich core is determined using classical beam theory. Second, the compressive fracture toughness of the lattice is calculated by the finite element (FE) method. For both the unnotched strength and fracture toughness, the competition between local failure criteria (tensile, compressive, and buckling) is explored. It is shown that the dominant mechanism is material dependent, and this is illustrated by appropriate material-property charts.

Third, a FE analysis of the stresses within the cracked sandwich plate is performed. It is recognised that the stresses remain bounded within the lattice in the  $K$ -dominated regime due to the finite cell size. Consequently, the stress concentration due to the presence of a crack in the lattice is finite. The magnitude of the stress concentration factor at the tip of the crack in the sandwich core is discussed. Analytical models are proposed to explain the fracture response of the sandwich plate with a cracked lattice core. These predictions are validated by extensive FE simulations, covering a wide range of crack length and lattice stockiness.

## 2. Unnotched strength of the sandwich core

### 2.1. Local tensile or compressive failure of the cell walls

Consider an infinitely long strip of diamond-celled lattice, sandwiched between rigid face-sheets, shown in [Fig. 2](#). The lattice is subjected to a remote compressive stress of magnitude  $\sigma_\infty$ . In the absence of a crack, the stress state within the lattice is determined by classical beam theory. The axial stress  $\sigma_a$  within each strut varies linearly across the section of each cell wall, and comprises the sum of a uniform stress over the section

$$\sigma_s = \frac{l}{t} \sigma_\infty \quad (3)$$

and a bending stress of amplitude

$$\sigma_b = \frac{3}{1 + (t/l)^2} \sigma_\infty \quad (4)$$

Consequently, the maximum compressive stress within the cell walls of the uncracked lattice is given by

$$\sigma_a = \frac{l + 3t}{t} \sigma_\infty \tag{5}$$

upon neglecting higher-order terms in  $t/l$ . The unnotched strength  $\sigma_u^C = \sigma_\infty$  of the sandwich plate for *local compressive failure* follows immediately by setting  $\sigma_a = \sigma_{CS}$ . It reads

$$\sigma_u^C = \frac{t}{l + 3t} \sigma_{CS} \tag{6}$$

Adequate accuracy is attained by neglecting the bending contribution at low relative densities ( $t/l < 0.05$ ), so that Eq. (6) reduces to

$$\sigma_u^C = \frac{t}{l} \sigma_{CS} \tag{7}$$

Now examine the possibility of *local tensile failure* under remote compressive loading. A cell wall within the lattice experiences tensile stresses when the amplitude of the bending component  $\sigma_b$  exceeds the compressive component  $\sigma_s$ . But this requires a high stockiness  $t/l > 0.38$ . We shall limit our study to slender lattices  $t/l < 0.38$ , and we thereby neglect the occurrence of local tensile fracture in the uncracked lattice subjected to macroscopic compressive loading.

### 2.2. Cell-wall buckling

The lattice core may also fail by elastic *buckling* of its cell walls. Preliminary finite element simulations reveal that the lowest eigenmode involves the co-operative rotation of joints such that each cell wall behaves as a pin-jointed Euler strut of length  $l$ , for which the buckling load is (Timoshenko and Gere, 1961) given by

$$P_{cr} = \frac{\pi^2 E_S I}{l^2} \tag{8}$$

with  $I = t^3/12$  per unit depth. Consequently, the unnotched compressive strength for local buckling is given by

$$\sigma_u^B = 0.82 \left(\frac{t}{l}\right)^3 E_S \tag{9}$$

Strictly, the above result is valid for a core of infinite height. The sensitivity of the buckling strength to the height  $2H$  of the sandwich core is explored by the finite element method in Appendix A. The main result is that Eq. (9) is adequate when the core contains more than about 6 cells in the height direction.

### 2.3. The dominant mechanism governing the unnotched strength of elastic–brittle lattice cores

It is instructive to explore the dependence of the active fracture micro-mechanism of lattice materials upon the constituent material properties. The unnotched strengths due to local compressive failure and due to elastic buckling are

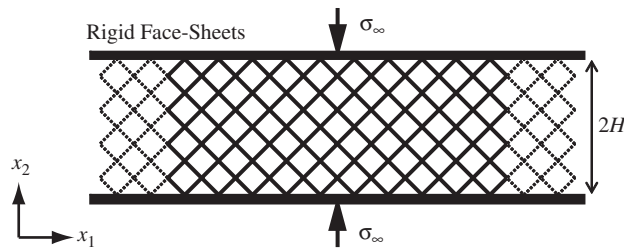


Fig. 2. Diamond-celled lattice core.

**Table 1**  
Unnotched strength of the sandwich core and fracture toughness of the diamond lattice.

Failure criterion	Unnotched strength	Fracture toughness
Tensile	–	$K_{IC}^T = 0.74tl^{-1/2} \sigma_{TS}$
Compressive	$\sigma_u^C = \frac{t}{l} \sigma_{CS}$	$K_{IC}^C = 0.44tl^{-1/2} \sigma_{CS}$
Buckling	$\sigma_u^B = 0.82 \left(\frac{t}{l}\right)^3 E_S$	$K_{IC}^B = 2 \left(\frac{t}{l}\right)^3 E_S \sqrt{l}$

The superscripts T, C, and B denote tension, compression, and buckling, respectively.

Please cite this article as: Quintana Alonso, I., Fleck, N.A., Compressive response of a sandwich plate containing a cracked diamond-celled lattice. J. Mech. Phys. Solids (2009), doi:10.1016/j.jmps.2009.05.008

summarised in Table 1. The transition from local buckling to local compressive failure is dependent upon the value of the non-dimensional group:

$$\Sigma \equiv \frac{\sigma_{CS}}{E_S} \left(\frac{l}{t}\right)^2 \quad (10)$$

We conclude from Table 1 that the unnotched strength is buckling governed when  $\Sigma > 0.82$ . This switch in behaviour is material dependent since  $\Sigma$  contains the material index  $\sigma_{CS}/E_S$ . This is made precise by plotting a material-property chart for elastic–brittle solids, with axes of  $\sigma_{CS}$  and  $E_S$ , see Fig. 3. We limit attention to solids of zero tensile ductility,  $\varepsilon_{TS} = 0$ , and show the data for a given class of materials (e.g. technical ceramics) in property envelopes, making use of CES (2007). The transition from local buckling to local compressive failure has been added to the map (dashed lines) for selected values of  $t/l$ .

For a slender lattice,  $t/l = 0.01$ , all materials possess a value of  $\Sigma$  above 0.82; consequently, the unnotched strength is governed by local buckling. In contrast, for stockier lattices in the range  $0.05 < t/l < 0.1$ , the lines of constant  $\Sigma$  cut through much of the data. There is an active competition between buckling and compressive failure of the cell walls, and the dominant failure mechanism is material dependent.

### 3. Compressive fracture toughness of the lattice

The FE method is now used to determine the mode I compressive fracture toughness of the diamond-celled lattice due to: (i) local compressive failure, (ii) local tensile failure, and (iii) local buckling of the cell walls. An analytical estimate of the buckling fracture toughness is then given.

The fracture toughness of the diamond lattice is evaluated by considering a cracked lattice subjected to an outer  $K$ -field, following Romijn and Fleck (2007). The displacement field  $u(x)$  associated with the  $K$ -field solution for an equivalent orthotropic elastic plate (Sih et al., 1965) is applied to the outer periphery of the lattice, see Fig. 4. Preliminary FE simulations revealed that the deformation field in the orthotropic lattice is characterised by narrow zones of intense bending emanating from the crack tip along the  $\pm 45^\circ$  directions, Fig. 4. The length  $\lambda$  of these bands is of order  $l^2/t$ . The FE code ABAQUS (version 6.7-1) was used to construct a mesh from beam elements. A mesh of size  $L = 600l$  ensures that the crack tip zone of bending of length  $\lambda$  is fully contained within the mesh. A single Euler–Bernoulli element (type B23 in ABAQUS notation) per strut suffices for the infinitesimal, linear response. However, numerical experimentation revealed that this type of beam element does not give accurate results in the post-buckling regime. To achieve adequate accuracy, 20 Timoshenko elements per strut are employed (of type B21 in ABAQUS notation).

A series of linear elastic FE simulations have been performed with  $t/l$  in the range  $5 \times 10^{-3}$  to 0.15. The displacements associated with a compressive  $K$ -field are applied to the periphery of the mesh. The maximum values of tensile stress and of compressive stress at any point in the lattice are plotted in Fig. 5 as functions of stockiness  $t/l$ . The mode I compressive fracture toughness for local compressive failure  $K_{IC}^C$  is obtained by equating the maximum compressive stress to the compressive strength  $\sigma_{CS}$  of the solid. The regression line of Fig. 5 gives

$$K_{IC}^C = 0.44t^{1/2}\sigma_{CS} \quad (11)$$

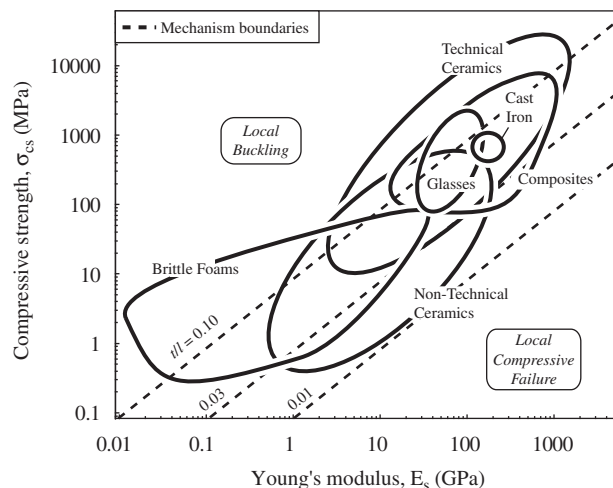
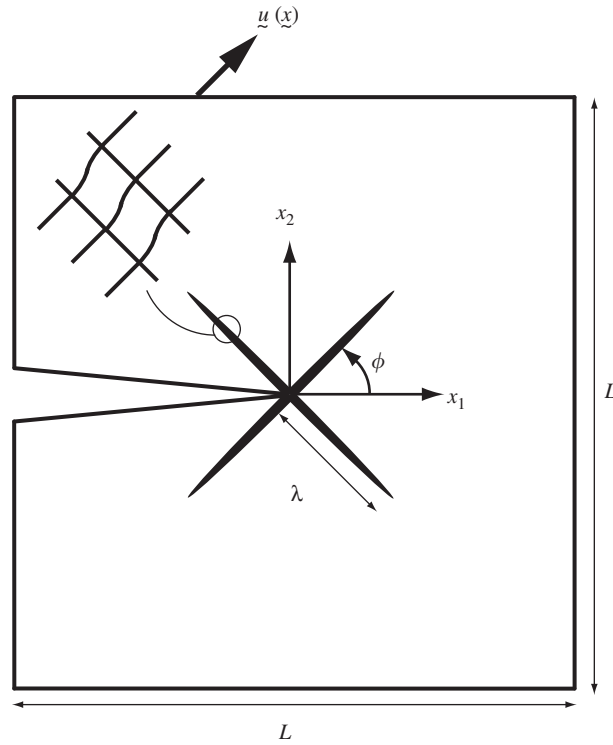


Fig. 3. Material-property chart for failure modes of unnotched lattice core.

Alternatively, the mode I compressive fracture toughness for *local tensile failure*  $K_{IC}^T$  is obtained by equating the maximum tensile stress at any point in the mesh to the tensile strength  $\sigma_{TS}$  of the solid. The FE simulations suggest that

$$K_{IC}^T = 0.74tl^{-1/2}\sigma_{TS} \quad (12)$$



**Fig. 4.** The boundary layer analysis used in the fracture toughness predictions. The crack tip is at the centre of the mesh. Shear bands of length  $\lambda$  align with the struts of the lattice.

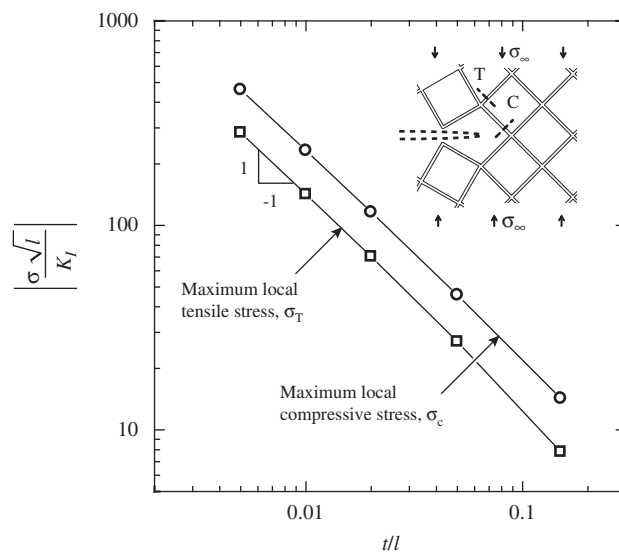


**Fig. 5.** Dependence of the maximum tensile stress  $\sigma_T$  and maximum compressive stress  $\sigma_C$  upon stockiness  $t/l$ . The sites of tensile failure (T) and compressive failure (C) are shown in the inset.

Predicted failure locations in the lattice are shown in the inset of Fig. 5. Local compressive failure takes place at site C, whereas local tensile failure takes place at site T. It is evident from Eqs. (11) and (12) that the dominant local failure mechanism depends upon the ratio of tensile to compressive fracture strength of the solid,  $\sigma_{TS}/\sigma_{CS}$ .

Alternatively, *local elastic buckling* may occur at the crack tip. An eigenvalue extraction is used in the FE calculations to determine the bifurcation load for buckling. The buckling fracture toughness  $K_{IC}^B$  was calculated for selected values of  $t/l$  and a regression analysis revealed that

$$K_{IC}^B = 2 \left( \frac{t}{l} \right)^3 E_S \sqrt{l} \tag{13}$$

The buckling behaviour was explored by performing additional FE simulations for the choice  $t/l = 0.01$ . The details are as follows. A finite deformation analysis was performed, employing small initial geometric imperfections of amplitude  $e$ . These imperfections were based on a linear superposition of the first 20 buckling eigenmodes, all weighted equally. The results are shown in Fig. 6, where the magnitude  $K_I$  of the applied compressive  $K$ -field is plotted against the maximum principal strain in the lattice. At sufficiently small values of the applied load  $K_I$ , the response is linear. At the bifurcation load  $K_I = K_{IC}^B$ , as given by Eq. (13), buckling initiates and in the post-buckling regime strut straining is significantly elevated. It is concluded that  $K_{IC}^B$  serves as a useful fracture parameter.

The *deformed meshes* of the fundamental equilibrium state and of the buckled state are shown in Fig. 7. The fundamental, pre-buckling path (Fig. 7a) is characterised by narrow bands of high bending stress emanating from the crack tip along  $\pm 45^\circ$  radial directions. The bands form as a result of the low ratio of shear modulus to direct modulus along these radial directions. They can be described as shear bands, and their length scales as  $l^2/t$ , in similar manner to that of the Kagome lattice, see Fleck and Qiu (2007). The 1st eigenmode (Fig. 7b) is anti-symmetric, whereas the 2nd eigenmode (Fig. 7c) is symmetric and occurs at a  $K$ -level about 35% higher than  $K_{IC}^B$ . At loads above the first eigenvalue, the full non-linear solution gives a deformation state close to that of the first eigenmode.

### 3.1. Analytical estimate of the buckling fracture toughness

An analytical model for the mode I tensile fracture toughness of the diamond-celled lattice has recently been developed by Quintana-Alonso and Fleck (2007a). The model can be used immediately to obtain the correct functional forms (11) and (12) for the compressive fracture toughness due to local compressive failure and local tensile failure, respectively. And, with some modification, the model can be used to obtain an estimate for the buckling fracture toughness  $K_{IC}^B$ . The strategy is to use the asymptotic stress field near the crack tip in the calculation for the buckling load of the critical strut.

Consider the cracked lattice shown in Fig. 8, and introduce the polar coordinate system  $(r, \theta)$ . Recall that the displacement field  $u_i$  associated with a  $K$ -field in an orthotropic elastic solid is (Sih et al., 1965) given by

$$u_i = \frac{K_I \sqrt{r}}{E_S} g_i(\theta, t/l) \tag{14}$$

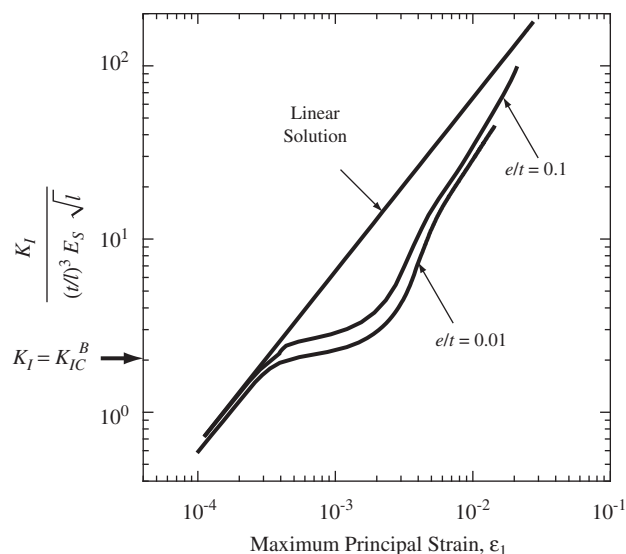


**Fig. 6.** The post-buckling response of a cracked lattice of stockiness  $t/l = 0.01$ . Initial geometric imperfections of amplitude  $e/t$  were present in the non-linear calculations.

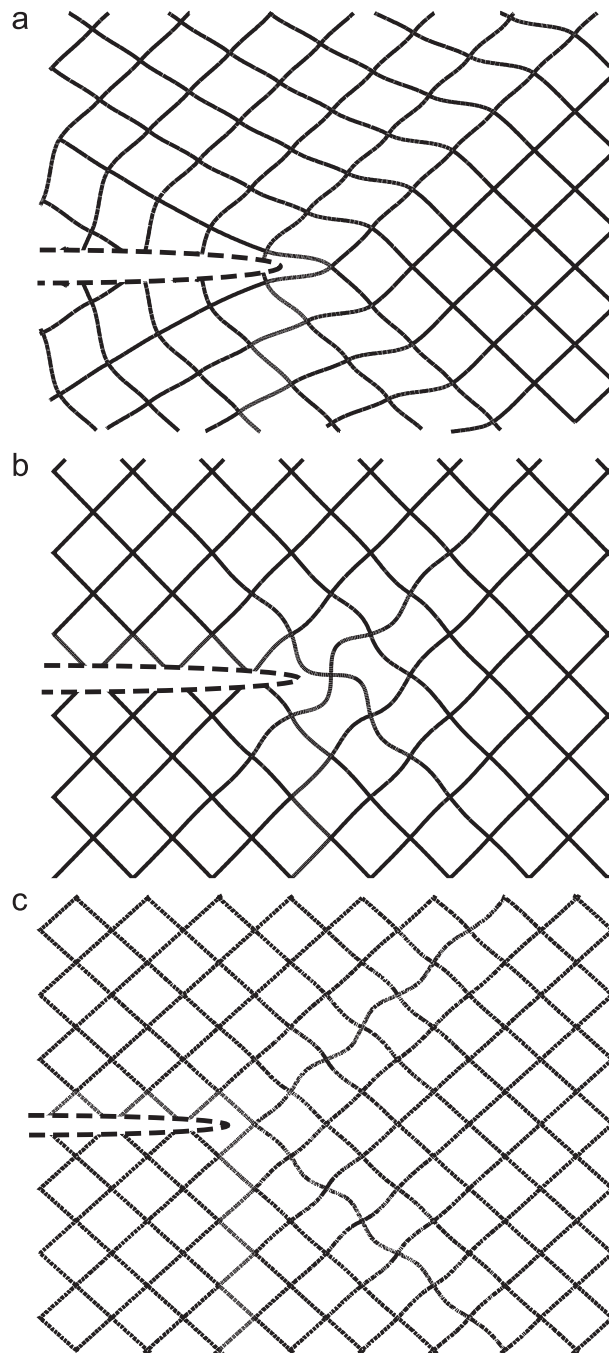


**Fig. 7.** Deformed mesh near the crack tip of a lattice subjected to a compressive  $K$ -field on its outer boundary. (a) Fundamental equilibrium path, showing shear zones of intense bending stresses. (b) First eigenmode and (c) second eigenmode, showing buckling of the near-tip struts.

where the non-dimensional function  $g_i(\theta, t/l)$  depends upon the angular co-ordinate  $\theta$  and upon the orthotropic properties of the continuum. The dependence on  $t/l$  enters because the ratio of shear modulus to direct modulus of the diamond lattice is a function of  $t/l$  (Romijn and Fleck, 2007).

The finite element simulations reported above indicate that local buckling of the crack tip struts follows the first eigenmode of Fig. 7b, and is detailed in Fig. 8. Evaluate the axial strain within the critical strut A–B of Fig. 8 by assuming that the macroscopic displacement field of Eq. (14) gives the local displacements of joints A and B located at the polar

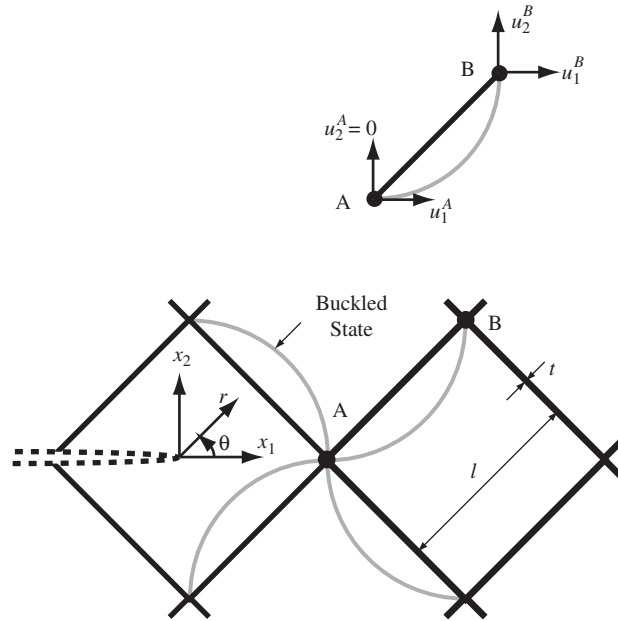


Fig. 8. The crack tip struts, showing the first eigenmode of buckling.

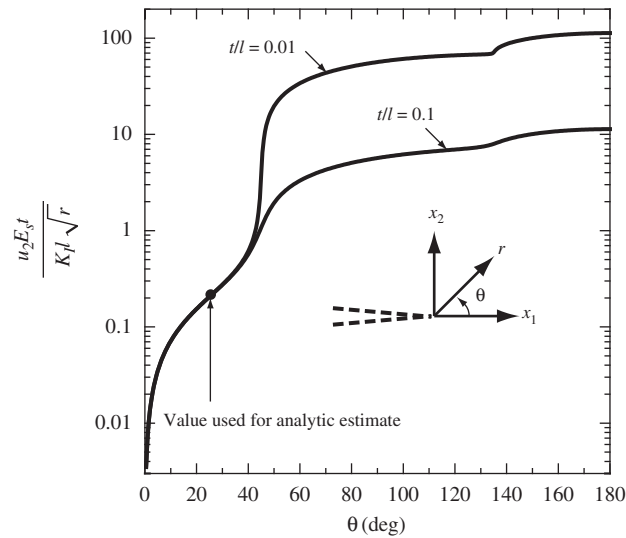


Fig. 9. Displacement  $u_2$  near the crack tip of an orthotropic elastic plate under mode I loading.

coordinates  $(l/\sqrt{2}, 0)$  and  $(l\sqrt{5}/2, \tan^{-1}(1/2))$ , respectively. The compressive axial strain in strut A–B reads

$$\varepsilon \approx 0.47 \frac{l^{1/2} K_I}{t E_S} \tag{15}$$

Now assume that this critical strut buckles as a pin-jointed Euler strut, and thus fails at an axial strain  $\varepsilon = \pi^2 t^2 / (12 l^2)$ . Consequently,

$$K_{IC}^B = 1.75 \left(\frac{t}{l}\right)^3 E_S \sqrt{l} \tag{16}$$

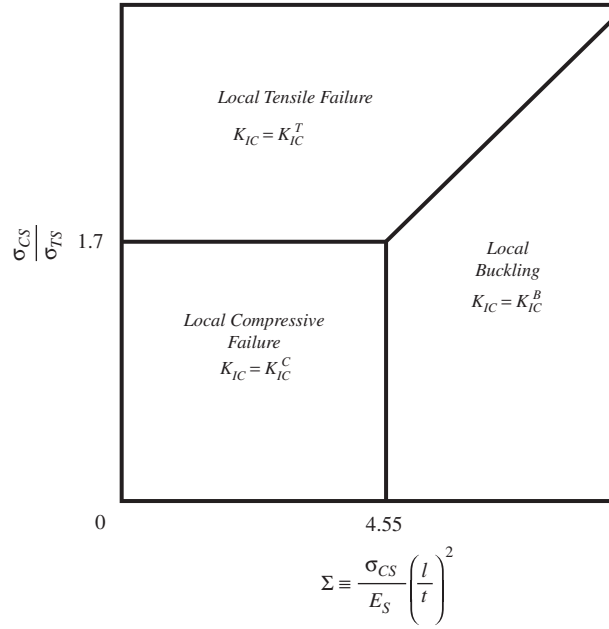


**Fig. 10.** Fracture mechanism map for compressive fracture toughness of the diamond lattice.

This simple analytical model provides the correct scaling law and requires only a minor correction to the numerical pre-factor in order to be brought into line with the numerical prediction of Eq. (13).

Note that Eq. (16) is based on an assumed form of the displacement field *ahead* of the crack tip. The same procedure based on the displacements *behind* the crack tip would erroneously predict that  $K_{IC}^B$  scales with  $(t/l)^4$ . This is traced to the fact that the displacement  $u_i$  scales as  $(t/l)^{-1}$  ahead of the crack tip, but as  $(t/l)^{-2}$  behind the crack tip. Further insight is gained by investigating the displacement field in a cracked orthotropic continuum. The component  $u_2 E_S t / (K_I l \sqrt{r})$  is plotted in Fig. 9 as a function of the polar co-ordinate  $\theta$ . It is evident that the displacement component scales as  $(t/l)^{-1}$  for  $|\theta| < 45^\circ$ . A narrow sector of intense strain occurs approximately at  $\theta = 45^\circ$ , and this manifests itself in the discrete lattice by the shear bands depicted in Fig. 7a. For  $|\theta| > 45^\circ$ , the displacements scale as  $(t/l)^{-2}$  and the normalisation used in Fig. 9 does not collapse the data for various  $t/l$ . The FE solutions for the discrete lattice similarly reveal that the displacement field scales as  $(t/l)^{-1}$  for  $\theta < 45^\circ$  and as  $(t/l)^{-2}$  for  $\theta > 45^\circ$  (not shown).

### 3.2. The competition between failure mechanisms for the compressive fracture toughness

The mode I compressive fracture toughness  $K_{IC}$  of the diamond-celled lattice is given by the minimum value of  $(K_{IC}^C, K_{IC}^T, K_{IC}^B)$  for any given stockiness and cell-wall material. Expressions (11)–(13) for the three competing failure modes are summarised in Table 1. We note that the local mechanism of failure at the crack tip depends upon the material index  $\sigma_{CS}/\sigma_{TS}$ , and upon the value of the non-dimensional group  $\Sigma \equiv \sigma_{CS} l^2 / (E_S t^2)$ . This competition between the local failure mechanisms that determine the compressive fracture toughness is illustrated in the fracture mechanism map of Fig. 10.

For any given  $t/l$ , the values of  $\Sigma$  and  $\sigma_{CS}/\sigma_{TS}$  are material dependent. Accordingly, a material-property chart can be constructed with axes  $\sigma_{CS}/E_S$  and  $\sigma_{CS}/\sigma_{TS}$ , see Fig. 11. The various classes of engineering solid have been added to the figure, and the boundaries between failure mechanisms have been included for selected values of  $t/l$ . Thus, the chart gives the active local failure mechanism for each class of solid. For example, cast irons lay mainly in the regime of elastic buckling  $K_{IC} = K_{IC}^B$  for slender lattices  $t/l = 0.01$ , but undergo local tensile failure for the case of a stockier lattice,  $t/l = 0.1$ . This property chart for compressive fracture toughness is the analogue of the chart given in Fig. 3 for the unnotched compressive strength. For any given material the local failure mechanism in a compressive fracture toughness test can be different from that in an unnotched compressive strength test.

It is instructive to compare the compressive fracture toughness  $K_{IC}$  with the usual tensile fracture toughness  $\tilde{K}_{IC}$  (associated with mode I crack opening), as given by Eq. (1). Fig. 11a has been re-plotted with the boundaries of compressive fracture mechanisms shown for  $t/l = 0.03$ , and contours of  $K_{IC}/\tilde{K}_{IC}$  have been added (Fig. 11b). Recall that the tensile fracture toughness  $\tilde{K}_{IC}$  is always dictated by local tensile failure of a material element near the crack tip. Consider first

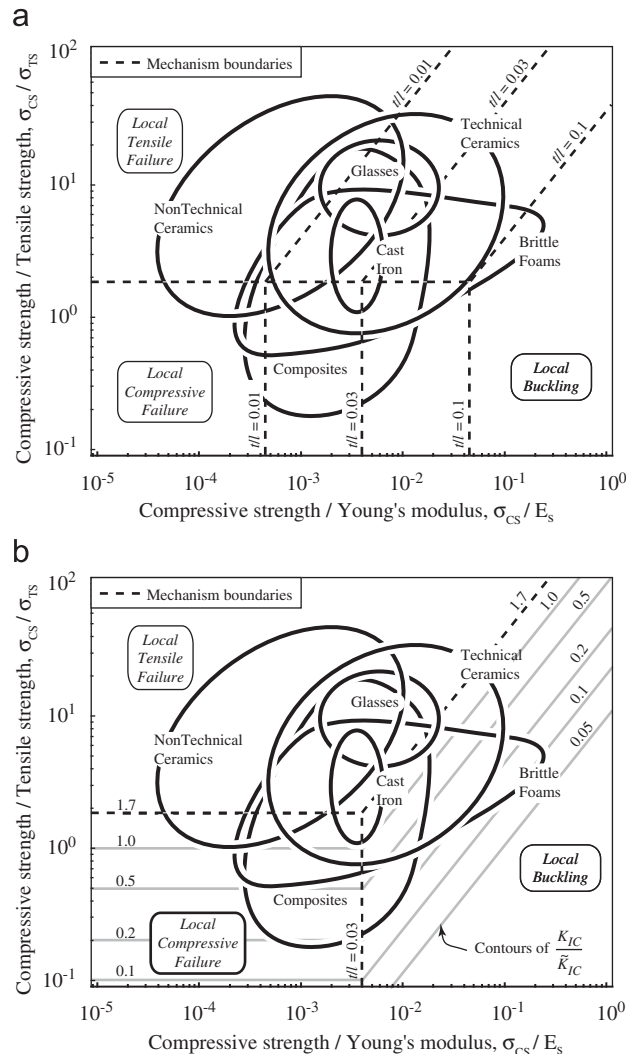


**Fig. 11.** Material-property chart for failure modes associated with the compressive fracture toughness of diamond lattice. The regimes of dominance for (a) selected values of  $t/l$  and for (b)  $t/l = 0.03$  with contours of  $K_{IC}/\tilde{K}_{IC}$ .

the case where the compressive fracture toughness  $K_{IC}$  is also dictated by local tensile failure. Then, the compressive fracture toughness  $K_{IC}$  is 70% above the tensile fracture toughness  $\tilde{K}_{IC}$ . Second, assume that local failure is by the attainment of the local compressive strength of the solid. Then, we have  $K_{IC}/\tilde{K}_{IC} = \sigma_{CS}/\sigma_{TS}$ . And third, when  $K_{IC}$  is governed by local buckling we obtain  $K_{IC}/\tilde{K}_{IC} = 4.55E_s t^2 / (\sigma_{TS} l^2)$ . Consequently, the compressive fracture toughness is much less than the tensile fracture toughness,  $K_{IC}/\tilde{K}_{IC} \ll 1$ , for lattices made from a solid of high tensile strength relative to the compressive strength and Young's modulus.

#### 4. Stress concentration factors for the cracked sandwich core

The reduction in macroscopic compressive strength due to the presence of the centre-crack in the diamond-celled lattice core of Fig. 1 can be assessed by means of the stress concentration introduced into the lattice by the presence of the crack. Consider the finite cracked geometry of Fig. 1, subjected to a gross compressive stress of magnitude  $\sigma_\infty$ . Write  $\sigma_C$  as the magnitude of the maximum compressive stress that arises anywhere in the lattice, and write  $\sigma_T$  as the magnitude of the maximum tensile stress at any point in the lattice. In order to evaluate the response of the cracked sandwich plate, we compare  $(\sigma_C, \sigma_T)$  with the magnitude  $\sigma_a$  of the maximum compressive stress in the unnotched lattice core also subjected to  $\sigma_\infty$  (Fig. 2). Recall that  $\sigma_a$  has already been given by Eq. (5). Accordingly, we define a stress concentration factor pertinent to

the local compressive failure mechanism, by

$$S_+ = \frac{\sigma_C}{\sigma_a}(1 - a/W) \geq 1 \tag{17}$$

and also define the stress concentration factor pertinent to the local tensile failure mechanism by

$$S_- = \frac{\sigma_T}{\sigma_a}(1 - a/W) \geq 0 \tag{18}$$

The term  $(1 - a/W)$  is included in the definitions of  $S$  in order to eliminate from  $S$  the stress enhancement associated with the reduction in net-section by the crack: we are interested in the stress magnification factor due to the presence of a crack,

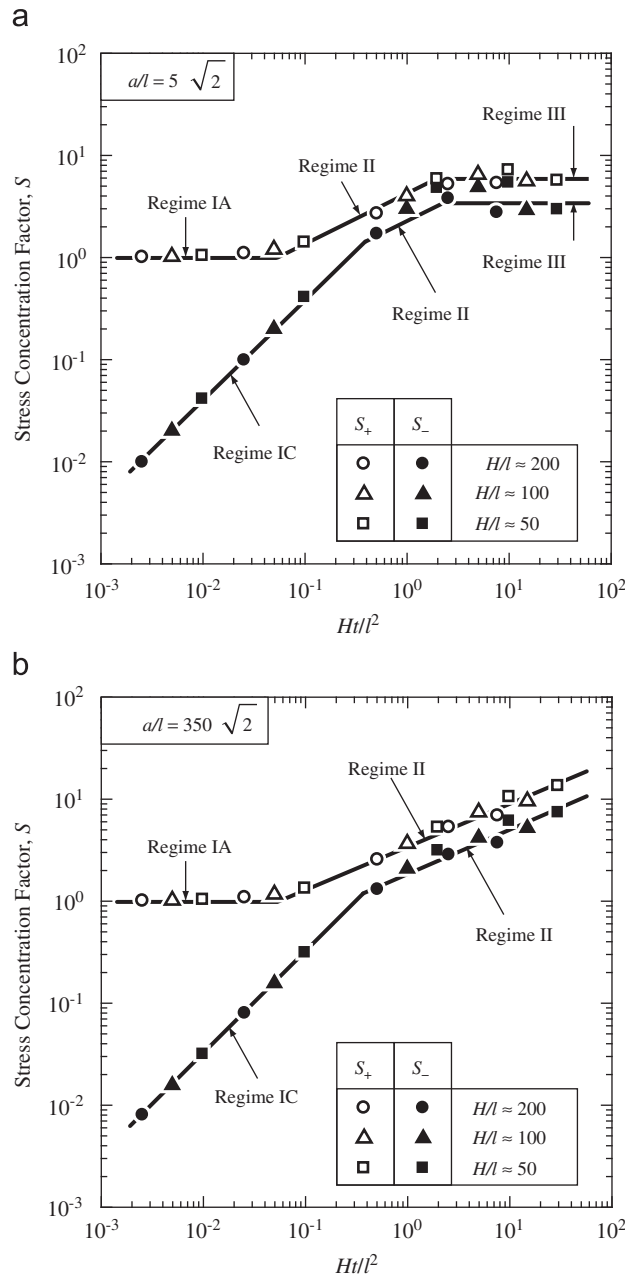


**Fig. 12.** Stress concentration factors ( $S_+$ ,  $S_-$ ) for crack lengths (a)  $a/l = 3\sqrt{2}$  and (b)  $a/l = 350\sqrt{2}$ . The solid lines denote analytic predictions derived from the expressions of Section 5. In all cases,  $W/l = 1400\sqrt{2} \approx 2000$ .

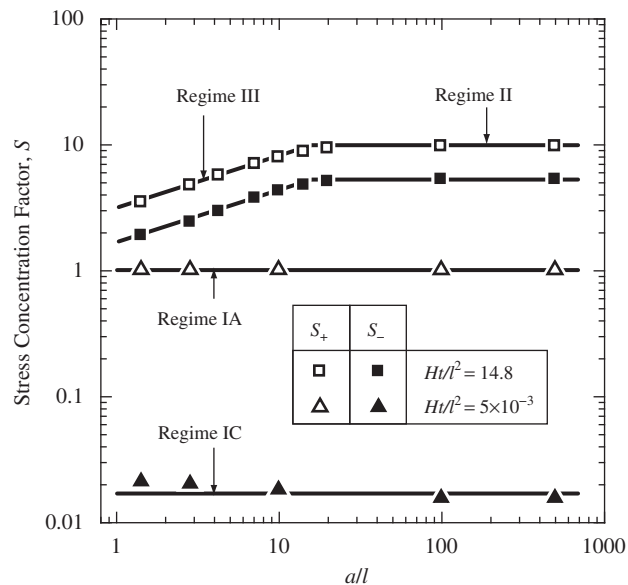


**Fig. 13.** Stress concentration factors ( $S_+$ ,  $S_-$ ) versus crack length, for extreme values of  $Ht/l^2$ . The solid lines denote analytic predictions derived from the expressions of Section 5.

over and above that due to the reduction in net-section. We emphasise that we take  $\sigma_a$  as the baseline reference stress in our definition of  $S$ . Thus,  $S_+ = 1$  when there is no stress concentration above the unnotched value. In general,  $S_+$  and  $S_-$  are functions of  $(t/l, a/l, H/l)$ .

#### 4.1. Numerical calculations

Linear-elastic FE calculations have been carried out to determine the stress concentration factors  $S_+$  and  $S_-$  of centrally cracked sandwich plates made from an elastic-brittle, diamond lattice. Selected crack lengths  $a/l$ , values of stockiness  $t/l$ , and specific geometries  $H/l$  have been used to analyse the response of the structure.

A finite element model of the cracked sandwich core was created using Euler-Bernoulli beam elements. For symmetry reasons only one quarter of the plate needed to be considered. A fixed aspect ratio  $W/l = 1400\sqrt{2} \approx 2000$  was used throughout the numerical study and it was ensured that  $H/W \leq 0.1$ . The crack in the lattice was created by splitting the joints along the cracking plane, while keeping intact the struts on either side, recall Fig. 1. The face-sheets were taken to be rigid, and were not modelled explicitly in the simulations. Rather, the lattice joints attached to the same face-sheet were subjected to the same prescribed vertical displacement  $u_2$ , along with zero rotation and zero horizontal displacement,  $\theta = u_1 = 0$ .

The dependence of  $(S_+, S_-)$  upon  $Ht/l^2$  are given in Fig. 12 for the extreme cases of a short crack,  $a/l = 3\sqrt{2}$ , and a long crack,  $a/l = 350\sqrt{2}$ . The simulations have been carried out by varying  $t/l$  over the range  $5 \times 10^{-5}$  to 0.15, for selected values of  $H/l$ . The choice of dimensionless group  $Ht/l^2$  for the abscissa collapses the data onto a single curve, for all values of  $H/l$ . The stress concentration factor for compressive local failure  $S_+$  ranges from unity at  $Ht/l^2 < 0.1$  to approximately 10 at high values of  $Ht/l^2$ . In contrast, the stress concentration factor for tensile local failure  $S_-$  varies from almost zero to about 10. The sensitivity of  $(S_+, S_-)$  to crack length is shown in Fig. 13 for two extreme values of  $Ht/l^2$ . The stress concentration factors are sensitive to  $a/l$  when the crack is short and  $Ht/l^2$  is large. Otherwise,  $(S_+, S_-)$  are insensitive to crack length. We shall make use of  $(S_+, S_-)$  in the following section in order to determine the compressive strength of the centre-cracked sandwich core, assuming that failure of the critical strut is by either local tensile fracture or compressive fracture. Additionally, we shall consider compressive failure due to local buckling near the crack tip.

Three distinct regimes of response are observed for the cracked sandwich plate, as highlighted by the solid lines in Fig. 12. The physical interpretation of each regime and the dependence of net section strength upon  $Ht/l^2$  and  $a/l$  within each regime is explored in the following section, making use of fracture mechanics concepts.

### 5. Regimes of behaviour of the cracked sandwich core

We shall now show that the compressive strength of the centre-cracked lattice core cannot be expressed simply in terms of the unnotched compressive strength and compressive fracture toughness of the lattice. A more complex approach is

needed as a consequence of the three competing modes of local failure (compressive fracture, tensile fracture, and local buckling). For any given material, the operative micromechanism of failure may change with change in geometry of the lattice core, such as  $t/l$ ,  $H/l$  or  $a/l$ . Simplification is possible, as the stress state within the cracked lattice is dictated by the values of  $Ht/l^2$ , with only a small role played by the value of  $a/l$ , recall Figs. 12 and 13. We proceed to describe simple analytical models for three asymptotic limits of value of  $Ht/l^2$  and  $a/l$ . A comparison with finite element simulations then reveals that the simple models are adequate over the full range of geometries considered for  $(t/l, a/l, H/l)$ . The three regimes are:

- (i) *Regime I*:  $Ht/l^2 \ll 1$  and any  $a/l$ ;
- (ii) *Regime II*:  $Ht/l^2 \gg 1$  and  $a/l > Ht/l^2$ ; and
- (iii) *Regime III*:  $Ht/l^2 \gg 1$  and  $a/l < Ht/l^2$ .

We consider each in turn.

### 5.1. Regime I

The stress state within the lattice core for Regime I is sketched in Fig. 14a. Elastic shear bands of high bending stresses emanate from the crack tip along the  $\pm 45^\circ$  directions, aligned with the lattice. The shear bands decouple the stress state ahead of the crack from the unloaded state along the crack flanks, with a negligible concentration of stress ahead of the crack tip. Recall that the finite element simulations in the boundary-layer, fracture toughness analysis of Section 3 reveal that the length of these bands is of order  $\lambda \propto l^2/t$ . Here, we consider the case where  $H/\lambda = Ht/l^2 \ll 1$  and so the elastic shear bands extend to the face-sheets.

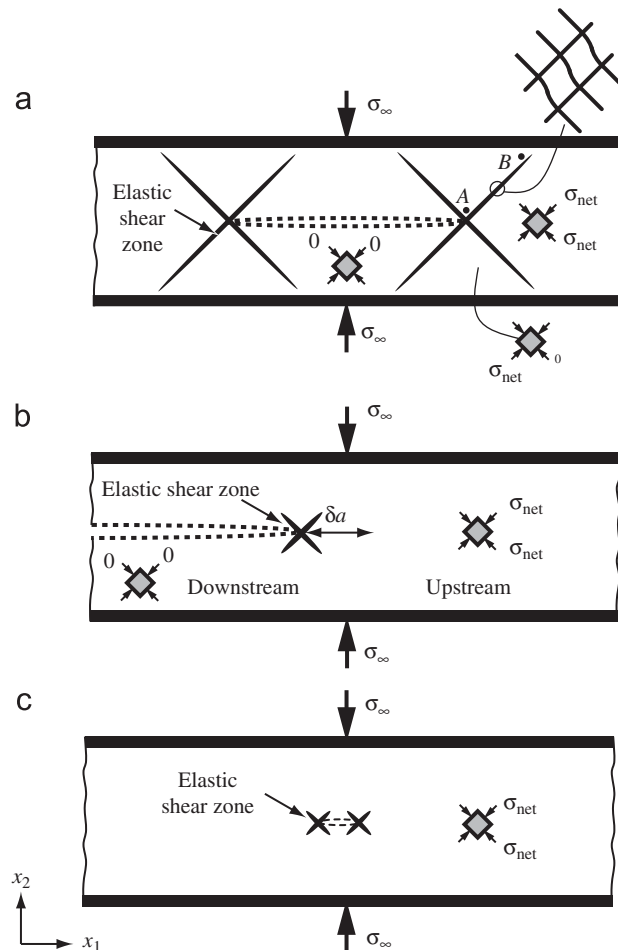


Fig. 14. Analytical models for (a) Regime I (b) Regime II, and (c) Regime III.

It is clear from Fig. 12 that  $S_+$  is close to unity for  $Ht/l^2 \ll 1$ , for both small and large  $a/l$ : the presence of the crack and attendant shear bands do not lead to an elevation of compressive stress within the lattice. Consequently, the sandwich core fails when the net section stress equals the unnotched compressive strength for this local failure mechanism, termed Regime IA. Likewise, the finite element calculations given below reveal that elastic buckling occurs when the net compressive stress attains the unnotched buckling strength of the lattice: the presence of the crack does not elevate the local compressive stress and so does not degrade the buckling strength. We write this failure regime as Regime IB.

In contrast, the presence of the elastic shear bands leads to bending of the struts and thereby to the presence of a local tensile stress. The shear bands emanating from the crack tip are blocked by the rigid face-sheets and a simple analytical model given below demonstrates that the level of bending stress scales with  $H/l$ . This is consistent with the fact that  $S_-$  scales linearly with  $Ht/l^2$  for  $Ht/l^2 \ll 1$ , recall Fig. 12. Although the magnitude of the tensile stress is much below the level of compressive stress within the lattice (that is  $S_- \ll S_+$ ), brittle solids such as ceramics have the property that their tensile strength  $\sigma_{TS}$  can be much less than their compressive strength  $\sigma_{CS}$ . Consequently, local tensile failure is a viable mechanism, and we refer to this as Regime IC. We emphasise that this tensile fracture mechanism requires the presence of a crack (of any length) within a shallow sandwich core ( $Ht/l^2 \ll 1$ ) and is not activated by compressive loading of an unnotched diamond lattice. Analytical models are presented in turn for the failure mechanisms of regimes IA, IB, and IC.

### 5.1.1. Regime IA

Local strut failure occurs in compression and no stress concentration is present,  $S_+ = 1$ . The net section strength of the plate  $\sigma_{net}^C$  is given by the unnotched strength,

$$\sigma_{net}^C = \sigma_u^C \quad (19)$$

with the magnitude of  $\sigma_u^C$  already stated in Eq. (7).

### 5.1.2. Regime IB

Elastic buckling occurs, again with no stress concentration at the crack tip. The net section failure strength for local buckling is given by

$$\sigma_{net}^B = \sigma_u^B \quad (20)$$

with  $\sigma_u^B$  defined in Eq. (9).

### 5.1.3. Regime IC

A tensile stress is generated within the bent struts of the shear band between the crack tip and the face-sheets (Fig. 14a). The magnitude of the maximum tensile stress is estimated by a shear lag analysis (Wicks and Guest, 2004), as follows. A deformed mesh is given in Fig. 15 where one of the shear bands is shown schematically. The line of struts AB is in the unloaded state since the node B is on the crack flank. In contrast, the axial compressive stress  $\sigma_{axial}$  within the neighbouring line of struts CD increases from C to D. Upon treating the lattice as an effective medium, the stress state ahead of the crack tip is equi-biaxial compression of magnitude  $\sigma_{net}$ . Consequently, the axial compressive stress within the strut at the crack tip node D has the maximum value of  $\sigma_{net}l/t$ .

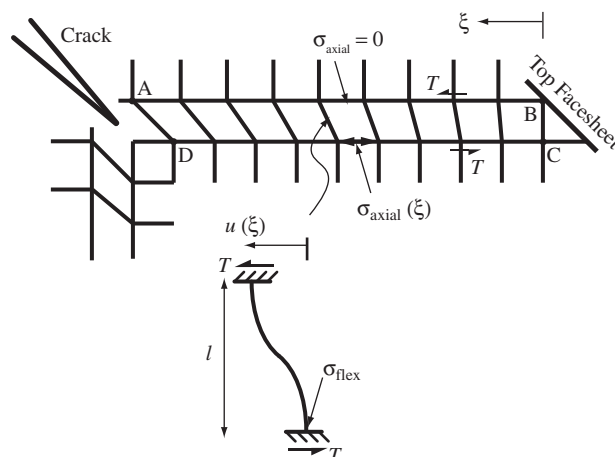


Fig. 15. Shear band model used to predict the tensile stresses within the elastic shear band for response IC.

Introduce the co-ordinate  $\xi$  as the distance along the shear band from the face-sheet at node C, such that  $\xi = H\sqrt{2}$  at point D, see Fig. 15. The shortening of the line of struts CD relative to the adjacent unloaded line of struts AB induces bending in the connecting struts, as sketched in Fig. 15. This array of bent struts within the shear band behaves as a line of springs, and elementary beam theory can be used to relate the shear traction  $T(\xi)$  to the shear displacement  $u(\xi)$  across the band, giving  $T = t^2 E_S u / l^4$ . The axial stress in the struts along the segment CD is  $\sigma_{axial} = E_S du / d\xi$ , while axial force equilibrium demands  $d\sigma_{axial} / d\xi = T$ . Consequently, we obtain a governing differential equation

$$\lambda^2 \frac{d^2 u}{d\xi^2} - u = 0 \tag{21}$$

where  $\lambda \equiv l^2 / t$  as before. This shear-lag equation has the following solution:

$$u(\xi) = \frac{\sigma_{net} l^3}{E_S t^2} \frac{\sinh(\xi / \lambda)}{\cosh(H\sqrt{2} / \lambda)} \tag{22}$$

upon making use of the boundary conditions  $u(0) = 0$  and  $\sigma_{axial} = E_S du / d\xi = \sigma_{net} l / t$  at  $\xi = H\sqrt{2}$ .

Now consider the flexural stress  $\sigma_{flex}$  within each bent strut. Beam theory provides the relation

$$\sigma_{flex}(\xi) = 3 \frac{t}{l^2} E_S u \tag{23a}$$

and consequently, the most heavily loaded strut connects nodes A and D at  $\xi = H\sqrt{2}$ , giving via (22),

$$\sigma_{flex}(H\sqrt{2}) = 3 \frac{l}{t} \sigma_{net} \tanh(Ht\sqrt{2} / l^2) \tag{23b}$$

The net tensile strength of the core  $\sigma_{net}^T$  follows immediately by equating  $\sigma_{flex}$  to  $\sigma_{TS}$ :

$$\sigma_{net}^T = \frac{1}{3} \frac{t}{l} \frac{\sigma_{TS}}{\tanh(Ht\sqrt{2} / l^2)} \tag{24a}$$

with asymptote

$$\sigma_{net}^T = \frac{1}{3\sqrt{2}} \frac{l}{H} \sigma_{TS} \tag{24b}$$

for small  $Ht / l^2$ . This asymptote can be immediately rewritten as

$$S_- = \frac{t}{l} \frac{\sigma_{TS}}{\sigma_{net}^T} = 3\sqrt{2} \frac{Ht}{l^2} \tag{25}$$

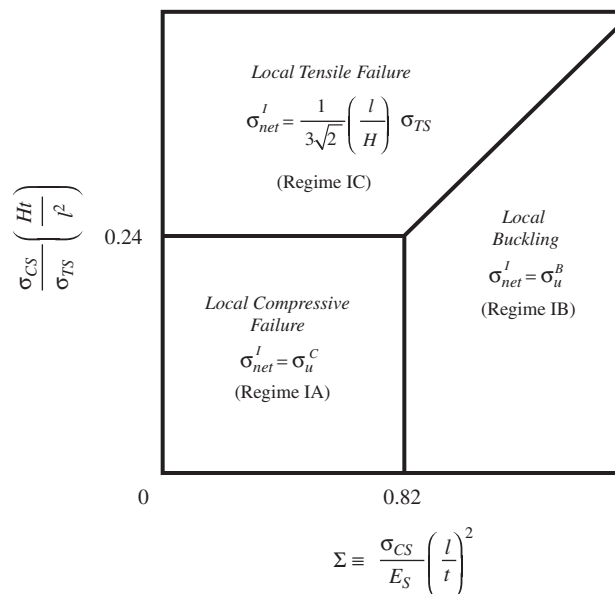


Fig. 16. Fracture mechanism map for Regime I.

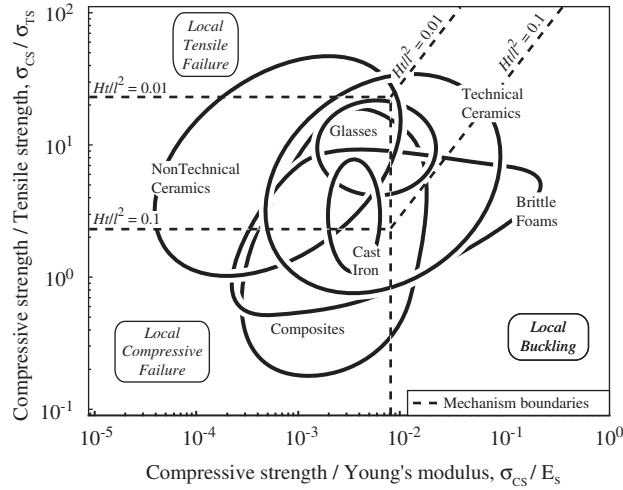


Fig. 17. Material-property chart for Regime I, with  $t/l = 0.1$ .

where  $S_-$  has already been defined in (18). Prediction (25) is in excellent agreement with the finite element predictions for  $S_-$  in Regime IC, recall Fig. 12.

In Regime I, the net-section strength  $\sigma_{net}$  is given by the unnotched strength of the core for local compressive failure, Eq. (19), and for local buckling, Eq. (20), and is given by the shear lag model for local tensile failure, Eq. (24b). The dominant fracture mechanism is determined by the lowest strength for any given geometry and the choice of material. It is instructive to plot the dominant fracture mechanism in the form of a map, see Fig. 16. The axes of the map are obtained by equating in pairs the expressions (7), (9), and (24b). The map gives the active local failure mechanism for Regime I, in terms of the sandwich geometry  $Ht/l^2$ , the material ratio  $\sigma_{CS}/\sigma_{TS}$ , and the non-dimensional group  $\Sigma \equiv \sigma_{CS} l^2 / (E_s t^2)$ .

The dominant fracture mechanism in Regime I for elastic–brittle engineering solids is explored in more detail in Fig. 17. The full range of brittle engineering solids are shown on a plot of  $\sigma_{CS}/\sigma_{TS}$  versus  $\sigma_{CS}/E_s$ . The regimes of dominance of the fracture mechanisms in Regime I are overlaid on the plot, upon taking the following specific choices for core geometry:  $t/l = 0.1$  and  $Ht/l^2 = 0.1, 0.01$ . It is clear that all three local failure mechanisms can occur in practice, and that for the same material the active failure micro-mechanism depends upon the assumed sandwich geometry. For example, local tensile failure (Regime IC) is inactive for a shallow lattice core ( $Ht/l^2 = 0.01$ ) made from glasses, but becomes feasible in deep glassy cores ( $Ht/l^2 = 0.1$ ).

## 5.2. Regime II

The length  $\lambda$  of the shear bands is now small relative to the height of the plate,  $\lambda \ll H$ . Additionally, the crack is sufficiently long compared to the core height that the core behaves as an orthotropic elastic strip with a semi-infinite crack, see Fig. 14b. Upstream of the crack tip, the lattice, treated as an effective medium, is in equi-biaxial compression, whereas downstream it is unloaded. A compressive  $K$ -field exists near the crack tip, with

$$K_I = F_I \sigma_{net} \sqrt{H} \quad (26)$$

in terms of the calibration function  $F_I = 2^{3/4}(t/l)^{1/2}$ , see Quintana-Alonso and Fleck (2007b).

Failure occurs when  $K_I$  attains the critical value  $K_{IC}$  as defined by the lowest value of Eqs. (11), (12), or (13). Consequently, we have

$$\sigma_{net}^C = 0.26 \frac{t}{l} \left( \frac{l^2}{Ht} \right)^{1/2} \sigma_{CS} \quad (27)$$

$$\sigma_{net}^T = 0.44 \frac{t}{l} \left( \frac{l^2}{Ht} \right)^{1/2} \sigma_{TS} \quad (28)$$

$$\sigma_{net}^B = 1.19 \left( \frac{t}{l} \right)^3 \left( \frac{l^2}{Ht} \right)^{1/2} E_s \quad (29)$$

where the superscripts  $T$ ,  $C$ , and  $B$  denote compressive, tensile, and buckling, respectively. Results (27) and (28) give

$$S_+ = \frac{3.85l}{(l+3t)} \left( \frac{Ht}{l^2} \right)^{1/2} \quad (30)$$

and

$$S_- = \frac{2.27l}{(l+3t)} \left( \frac{Ht}{l^2} \right)^{1/2} \quad (31)$$

respectively. The agreement with finite element simulations is excellent, see Figs. 12 and 13.

### 5.3. Regime III

The crack is now much smaller than the height and width of the sandwich plate, as illustrated in Fig. 14c. The  $K$ -calibration for an orthotropic plate containing a short centre-crack of length  $2a$  is approximately

$$K_I = \sigma_{net} \sqrt{\pi a} \quad (32)$$

as discussed by Quintana-Alonso and Fleck (2007b). Upon equating  $K_I$  to  $K_{IC}$  we obtain via (11)–(13),

$$\sigma_{net}^C = 0.24 \frac{t}{l} \left( \frac{l}{a} \right)^{1/2} \sigma_{CS} \quad (33)$$

$$\sigma_{net}^T = 0.42 \frac{t}{l} \left( \frac{l}{a} \right)^{1/2} \sigma_{TS} \quad (34)$$

$$\sigma_{net}^B = 1.13 \left( \frac{t}{l} \right)^3 \left( \frac{l}{a} \right)^{1/2} E_S \quad (35)$$

Expressions (33) and (34) give

$$S_+ = \frac{4.17l}{(l+3t)} \left( \frac{a}{l} \right)^{1/2} \quad (36)$$

and

$$S_- = \frac{2.38l}{(l+3t)} \left( \frac{a}{l} \right)^{1/2} \quad (37)$$

respectively. Again, the agreement with finite element simulations is excellent, recall Figs. 12 and 13.

We emphasise that Regimes II or III occur when  $Ht/l^2 \gg 1$ . A comparison of (27)–(29) with (33)–(35) suggests that Regime II dominates for  $a/l > Ht/l^2$ , while Regime III dominates for  $a/l < Ht/l^2$ .

## 6. A systematic procedure for determining the compressive strength of a centre-cracked lattice core for any given material and geometry

It remains to provide a systematic procedure in order to obtain the compressive strength  $\sigma_{net}$  of a sandwich plate with a centre-cracked lattice core. Consider a cracked geometry as specified by  $(a/l, Ht/l^2, \sigma_{CS}/\sigma_{TS}, \Sigma \equiv \sigma_{TS}^2 l^2 / (E_S t^2))$ . We assert that failure occurs in Regimes I, II or III, despite the fact that these regimes were introduced in Section 5 as asymptotic responses at either small or large  $Ht/l^2$ . The justification for this is given by a comprehensive set of FE calculations, summarised in Appendix B.

In principle, a map to show the domains of dominance of Regimes I, II, or III could be developed with axes  $(a/l, Ht/l^2)$ , for any assumed values of  $(\sigma_{CS}/\sigma_{TS}, \Sigma)$ . (Such an approach was adopted by Quintana-Alonso and Fleck (2007b) for the tensile fracture of a cracked sandwich core.) The following major simplification can be made for the compression problem over the practical range of values of  $(\sigma_{CS}/\sigma_{TS}, \Sigma)$  as given in Fig. 3. Introduce a transition core height  $(Ht/l^2)_{trans}$ , to be made precise below. Then,

- (i) Regime I is active for  $Ht/l^2 < (Ht/l^2)_{trans}$ ,
- (ii) Regime II is active for  $(Ht/l^2)_{trans} < Ht/l^2 < a/l$ , and
- (iii) Regime III is active for  $Ht/l^2 > a/l$ .

The value of  $(Ht/l^2)_{trans}$  is obtained by equating the strength  $\sigma_1$  in Regime I with the strength  $\sigma_2$  in Regime II. This transition value is independent of  $a/l$  but is a function of  $(\sigma_{CS}/\sigma_{TS}, \Sigma)$ , as follows.

**Table 2**

Transition value  $(Ht/l^2)_{trans}$  between Regimes I and II (which depends upon the local failure mode dictating each fracture domain).

	REGIME II		
	Compressive	Buckling	Tensile
REGIME I			
Compressive (IA)	0.07	Not viable	0.19 $(\sigma_{TS}/\sigma_{CS})^2$
Buckling (IB)	0.1 $\Sigma^2$	2.1	0.29 $(\Sigma\sigma_{TS}/\sigma_{CS})^2$
Tensile (IC)	0.82 $(\sigma_{TS}/\sigma_{CS})^2$	0.04 $(\Sigma\sigma_{TS}/\sigma_{CS})^2$	0.29

The non-dimensional group  $\Sigma$  was defined in Section 2.3 as  $\Sigma = \sigma_{CS} l^2 / (E_s t^2)$ .

First, consider the strength-controlled Regime I, and identify the weakest mode of local failure using the criteria summarised in Fig. 16. Denote the associated strength  $\sigma_1$ . Note that  $\sigma_1$  is expressed in terms of  $Ht/l^2$  for Regime IC, but is independent of  $Ht/l^2$  for Regimes IA and IB.

Second, consider Regime II and note that the value of compressive fracture toughness  $K_{IC}$  depends upon the local active mechanism. The competition is detailed in the fracture toughness map of Fig. 10, and the expressions for each local failure mechanism are summarised in Table 1. Now calculate the net-section strength  $\sigma_2 = \sigma_{net}$  for Regime II via Eq. (26).

The value of  $(Ht/l^2)_{trans}$  follows immediately by equating  $\sigma_1$  and  $\sigma_2$ . Expressions for the transition value have been determined for all possible local mechanisms in Regimes I and II, and the resulting expressions for  $(Ht/l^2)_{trans}$  are listed in Table 2.

## 7. Concluding remarks

The compressive fracture response has been explored for a sandwich plate with a centre-cracked core made from an elastic–brittle, diamond-celled lattice. Analytical models and extensive finite element simulations show that the behaviour can be adequately represented by three regimes of response in terms of sandwich geometry. Regime I exists for  $Ht/l^2 \ll 1$ , and is characterised by shear bands that span between the crack tip and face-sheets. For any crack length, there is a negligible concentration of compressive stress within the lattice, but tensile stresses arise within the bent struts of the band. In Regimes II and III, a  $K$ -field develops and conventional linear elastic fracture mechanics applies. Regime II exists for long cracks compared with the height of the sandwich plate, and Regime III, for short cracks.

Microstructural imperfections in the form of missing struts, misplaced joints, and wavy cell walls are expected to have an additional knockdown effect upon the fracture properties of elastic–brittle lattices. In broad terms, the imperfection sensitivity of 2D lattices is dictated by the nodal connectivity (Symons and Fleck, 2008). A connectivity of 4, as in the diamond-celled lattice of this study, is the transition case: the behaviour of structure can be bending or stretching dominated depending on the degree of imperfection. Consequently, the fracture toughness of the diamond lattice is imperfection-sensitive. Romijn and Fleck (2007) have recently explored the sensitivity of fracture toughness of several 2D lattices to a random distribution of misplaced joints. They show that the diamond lattice exhibits a significant degradation of its fracture properties due to the presence misplaced joints. The knockdown is greatest for slender lattices. For example, in a lattice of stockiness  $t/l = 0.01$ , the misplacement of nodes by one tenth of the cell size decreases the tensile fracture toughness by a factor of approximately two. These results can be used directly in the above strength predictions for the cracked sandwich plate. Thereby, the role of imperfections at the cell-wall level can be incorporated into the analysis.

## Appendix A. Unnotched buckling strength

The buckling load predicted by Eq. (9) is the bifurcation load of an infinite lattice under equi-biaxial loading (Fig. A1). This analytic prediction has been validated by an FE eigenvalue extraction using the commercial code ABAQUS (version 6.7-1). Each cell wall was meshed with 20 Timoshenko beam elements (type *B21* in ABAQUS notation). Periodic boundary conditions were applied to the edges of the sandwich geometry, such that displacements and rotations on the left (*L*) and right (*R*) edges were equal:  $u_1^L = u_1^R$ ;  $u_2^L = u_2^R$ ;  $\theta^L = \theta^R$ . The face-sheets were not allowed to rotate or to displace in the transverse direction. The effect of a varying height  $2H$  is investigated for a mesh of fixed width  $W/l = 70\sqrt{2} \approx 100$ . A representative FE model and the observed buckling mode are shown in Fig. A1.

Fig. A2 shows the buckling load  $\sigma_{peak}$  obtained from the FE eigenvalue analysis plotted against  $H/l$ . For  $H/l \approx 1.5$  the buckling load predicted by the FE is about twice that of Eq. (9). This is attributed to the effect of the thin elastic boundary layer that forms at the faces of the sandwich plate, as revealed by the FE simulation shown in Fig. A1. Deformation is restricted adjacent to the face-sheets. The boundary layer effect decays rapidly with increasing height, and for about

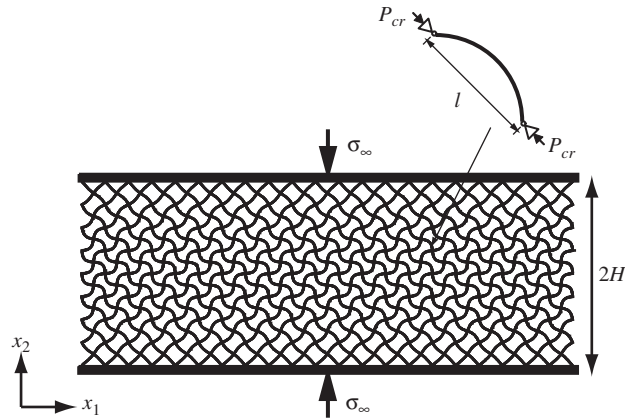


Fig. A1. Buckling of an unnotched plate subjected to remote compression.

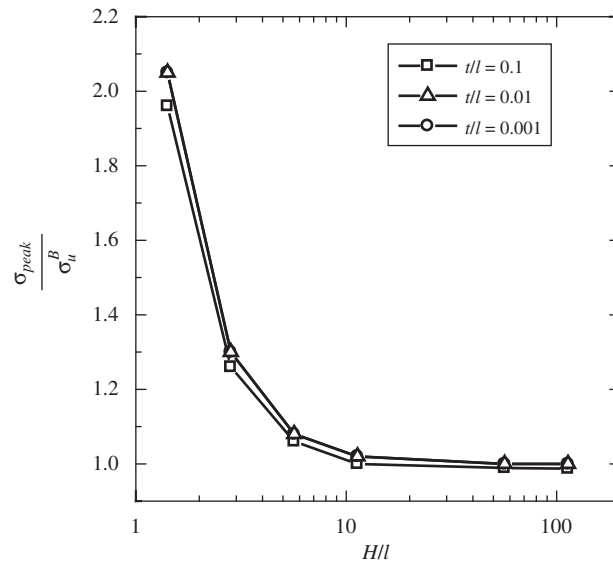


Fig. A2. Effect of specimen height  $2H$  upon the buckling strength of the unnotched sandwich core.

$H/l > 10$  the buckling load of the sandwich plate is accurately predicted by Eq. (9). The depth of the boundary layer is on the order of the cell size and is independent of strut stockiness (Fig. A2).

## Appendix B. Finite element validation of the regimes of behaviour

Extensive FE simulations have been performed to validate the analytical predictions of Section 5. A finite element model of the cracked sandwich core was created using Euler–Bernoulli beam elements. The model had fixed aspect ratios  $H/l = 70\sqrt{2} \approx 100$  and  $H/W = 1/20$ . The morphology of the crack and the applied load were defined in the manner described in Section 4. We investigate the sensitivity of the net-section strength of the sandwich plate to crack size  $a/l$  and stockiness  $t/l$ .

To validate the strength predictions it is useful to consider each of the three local failure criteria in turn. For local compressive failure and local tensile failure, linear elastic calculations are used. For local buckling, an eigenvalue analysis of the centre-cracked plate is conducted.

### B1. Local compressive failure

Assume local failure of the lattice occurs by the attainment of the *compressive* strength of the solid material. The strength of the sandwich plate is determined from a series of FE linear elastic calculations by examining the maximum

compressive stress anywhere in the lattice. The results are shown in Fig. B1 for the choice of crack lengths  $a/l = 5\sqrt{2}$  and  $a/l = 700\sqrt{2}$ , and stockiness values  $t/l$  in the range  $5 \times 10^{-5}$  to 0.2. We note from Table 1 that the unnotched strength for local compressive failure is approximately  $\sigma_u^c = (t/l)\sigma_{CS}$  when  $t/l$  is small, and so the net strength has been normalised by  $(t/l)\sigma_{CS}$  in Fig. B1. Analytical predictions are included as solid lines, using Eq. (19) in Regime IA, Eq. (27) in Regime II, and Eq. (33) in Regime III. Excellent agreement between the analytical formulae and the numerical predictions is observed for all three Regimes of behaviour.

The transitions between the regimes of behaviour are obtained by equating the appropriate expressions of strength. The transition between Regimes IA and II is at  $(Ht/l^2)_{trans} = 0.07$ , as listed in Table 2. The FE simulations confirm that below a transition value  $Ht/l^2 < 0.07$ , the response lies within Regime IA: there is no stress concentration at the crack tip and  $\sigma_{net}^c \approx \sigma_u^c$ . Above this transition value, the response is toughness-controlled: there is stress intensification at the crack tip and the net-strength is below the unnotched value. In Regime II, the normalised strength of the plate is independent of crack length and scales as  $(l^2/Ht)^{1/2}$ , recall Eq. (27). In Regime III, the normalised strength is independent of stockiness and scales with crack length according to  $(l/a)^{1/2}$ , as given by Eq. (33).

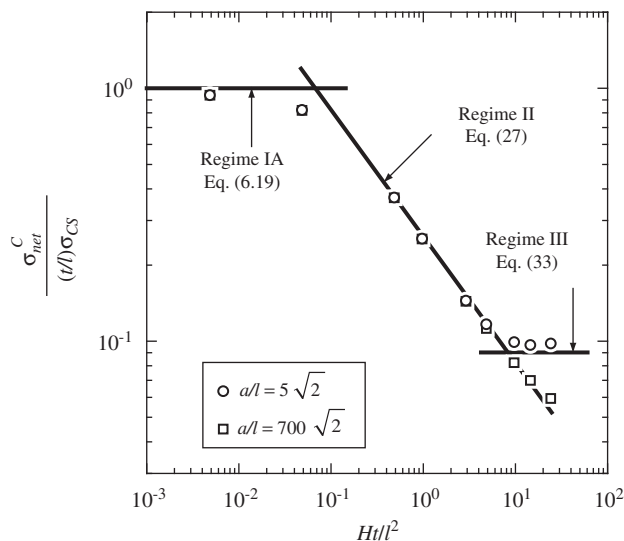


Fig. B1. Net-section strength for local compressive failure plotted against stockiness.  $H/l = 70\sqrt{2} \approx 100$ ,  $W/H = 20$ .

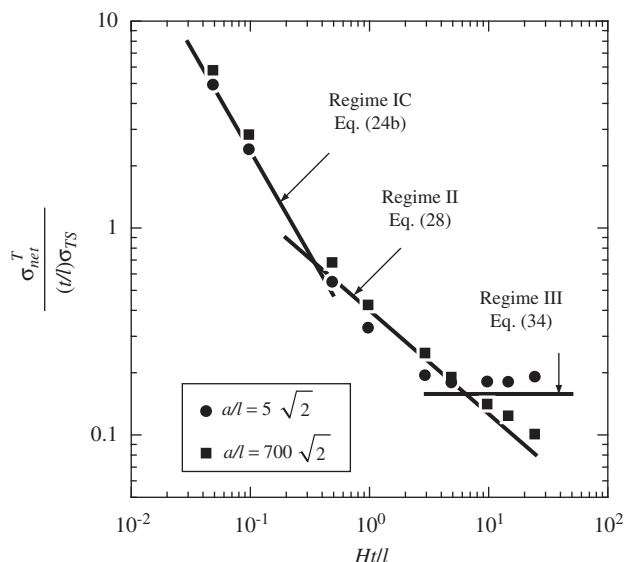


Fig. B2. Net-section strength for local tensile failure plotted against stockiness.  $H/l = 70\sqrt{2}$ ,  $W/H = 20$ .

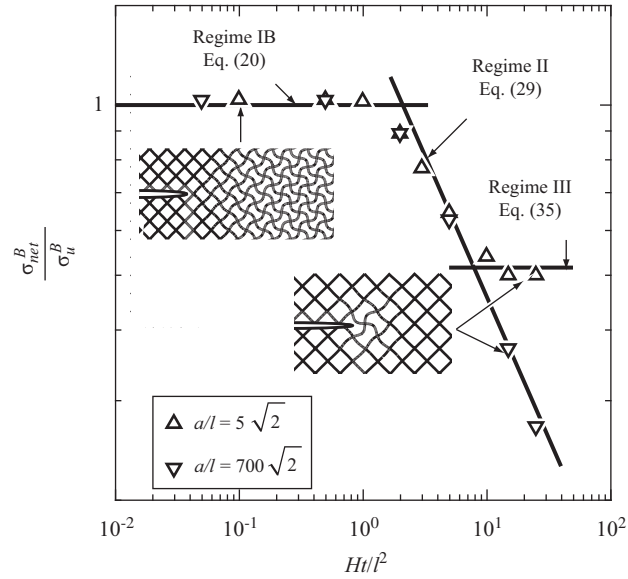


Fig. B3. Buckling strength of the cracked core.  $H/l = 70\sqrt{2}$ ,  $W/H = 20$ .

The above FE study has been repeated for a wide range of crack lengths spanning from  $a/l = \sqrt{2}$  to  $a/l = 700\sqrt{2}$ . The accuracy of the analytical predictions is comparable to that demonstrated in Fig. B1. These results are omitted here for the sake of brevity.

### B2. Local tensile failure

Now assume that local failure of the lattice occurs by attainment of the *tensile* strength of the solid. The strength of the sandwich plate is determined from the FE simulations by examining the maximum tensile stress at any point in the lattice. Fig. B2 shows the normalised net-section strength  $\sigma_{net}^T / (\sigma_{TST}/l)$  plotted against  $Ht/l^2$  for the choice  $a/l = 5\sqrt{2}$  and  $a/l = 700\sqrt{2}$ . Again, close agreement is noted between analytical predictions and numerical calculations for all regimes of behaviour. The transition between Regimes IC and II is at  $(Ht/l^2)_{trans} = 0.29$ , see Table 2. The results support the existence of Regime IC for  $Ht/l^2 < 0.29$ . The normalised strength in Regime IC is inversely proportional to the height of the plate and the stockiness of the lattice, scaling as  $l^2/Ht$ , recall Eq. (24b). With increasing  $Ht/l^2$  the response switches to Regime II and the normalised strength scales with  $(l^2/Ht)^{1/2}$ , in accordance with Eq. (28). And at large  $Ht/l^2$ , the response for the short crack is given by Regime III, such that the normalised strength is insensitive to  $Ht/l^2$ , as derived from Eq. (34).

### B3. Local buckling

Assume that failure is by local buckling of the cell walls. In order to validate the strength predictions an eigenvalue extraction of the centre-cracked sandwich plate has been conducted. The bifurcation stress  $\sigma_{net}^B$  normalised by the buckling strength of the unnotched core  $\sigma_u^B$  is plotted against  $Ht/l^2$  in Fig. B3. The FE data are accurately predicted by Eq. (20) in Regime IB, Eq. (29) in Regime II, and Eq. (35) in Regime III. The transition between Regimes IB and II is given by  $(Ht/l^2)_{trans} = 2.1$ , as reported in Table 2. At  $Ht/l^2$  values above 2.1, the strength is dictated by the toughness of the lattice: in Regime II the normalised strength  $\sigma_{net}^B / \sigma_u^B$  scales as  $(l^2/Ht)^{1/2}$  and is independent of crack length, while in Regime III it scales as  $(l/a)^{1/2}$  and is independent of stockiness. At  $Ht/l^2$  below 2.1, Regime IA dominates and the unnotched buckling strength of the panel is recovered,  $\sigma_{net}^B = \sigma_u^B$ . The transition between toughness-control to strength-control is associated with a switch in buckling mode of the lattice, see the inserts of Fig. B3. In Regime IB, buckling occurs uniformly throughout the core of the sandwich plate, whereas in Regimes II and III, a  $K$ -field develops and only the near-tip struts buckle.

Full non-linear FE calculations of selected geometries have also been carried out to confirm the buckling loads obtained from the eigenvalue analysis. The limit loads attained were equal to the bifurcation loads presented in Fig. B3. The excellent agreement between FE results and simple analytical models corroborates the applicability of the buckling fracture toughness  $K_{IC}^B$  as a useful fracture parameter. It is remarkable that the simple estimates based on LEFM for a continuum capture the response in Regimes II and III, despite the fact that the crack extends over only a few broken cells.

## References

- CES EduPack, 2007. The Cambridge Engineering Selector. Granta Design, Rustat House, 62 Clifton Road, Cambridge CB1 7EG, UK.  
Christensen, R.M., 2000. Mechanics of cellular and other low-density materials. *Int. J. Solids Struct.* 37 (1–2), 93–104.

- Côte, F., Deshpande, V.S., Fleck, N.A., Evans, A.G., 2006. The compressive and shear responses of corrugated and diamond lattice materials. *Int. J. Solids Struct.* 43 (20), 6220–6242.
- Gibson, L.J., Ashby, M.F., 1997. *Cellular Solids: Structure and Properties*, second ed. Pergamon Press, Oxford, UK.
- Gulati, S.T., 1975. Effects of cell geometry and thermal shock resistance of catalytic monoliths. SAE Paper No. 750171.
- Gulati, S.T., 1983. Thermal stresses in ceramic wall-flow diesel filters. SAE Paper No. 830079.
- Fleck, N.A., Kang, K.J., Ashby, M.F., 1994. The cyclic properties of engineering materials. *Acta Metall. Mater.* 42 (2), 365–381.
- Fleck, N.A., Qiu, X., 2007. The damage tolerance of elastic–brittle, two dimensional isotropic lattices. *J. Mech. Phys. Solids.* 55 (3), 562–588.
- Huang, J.S., Gibson, L.J., 1991. Fracture toughness of brittle honeycombs. *Acta Metall. Mater.* 39 (7), 1617–1626.
- Lipperman, F., Rvkin, M., Fuchs, M.B., 2007. Fracture toughness of two-dimensional cellular material with periodic microstructure. *Int. J. Fract.* 146, 279–290.
- Mora, R.J., Waas, A.M., 2002. Strength scaling of brittle graphitic foam. *Proc. R. Soc. Lond. A* 458, 1695–1718.
- Quintana-Alonso, I., Fleck, N.A., 2007a. Damage tolerance of an elastic–brittle diamond-celled honeycomb. *Scr. Mater.* 56 (8), 693–696.
- Quintana-Alonso, I., Fleck, N.A., 2007b. The damage tolerance of a sandwich panel containing a cracked honeycomb core. *J. Appl. Mech.* In press.
- Quintana-Alonso, I., Mai, S.P., Fleck, N.A., Oakes, D.C.H., Twigg, M.V., 2009. The fracture toughness of a cordierite square lattice. *Acta Mater.*, submitted for publication.
- Romijn, N.E.R., Fleck, N.A., 2007. The fracture toughness of planar lattices: imperfection sensitivity. *J. Mech. Phys. Solids* 55 (12), 2538–2564.
- Scheffler, M., Colombo, P. (Eds.), 2005. *Cellular Ceramics: Structure, Manufacturing, Properties and Applications*. Wiley-VCH, Weinheim.
- Sih, G.C., Paris, P.C., Irwin, G.R., 1965. On cracks in rectilinearly anisotropic bodies. *Int. J. Fract. Mech.* 1 (3), 189–203.
- Symons, D.D., Fleck, N.A., 2008. The imperfection sensitivity of isotropic two-dimensional elastic lattices. *J. Appl. Mech.* 75 (5).
- Timoshenko, S.P., Gere, J.M., 1961. *Theory of Elastic Stability*, second ed. McGraw-Hill, New York.
- Valdevit, L., Hutchinson, J.W., Evans, A.G., 2004. Structurally optimized sandwich panels with prismatic cores. *Int. J. Solids Struct.* 41, 5105–5124.
- Wadley, H.N.G., 2006. Multifunctional periodic cellular metals. *Philos. Trans. R. Soc. A* 364 (1838), 31–68.
- Wang, A.-J., McDowell, D.L., 2004. In-plane stiffness and yield strength of periodic metal honeycombs. *J. Eng. Mater. Technol.* 126 (2), 137–156.
- Wicks, N., Guest, S., 2004. Single member actuation in large repetitive truss structures. *Int. J. Solids Struct.* 41, 965–978.